Transport and Communications Science Journal

ANALYSIS OF SLOPE STABILITY UNDER DYNAMIC VEHICLE LOADS INDUCED BY ROUGH FLEXIBLE PAVEMENTS

Huynh Van Quan

Campus in Ho Chi Minh City, University of Transport and Communications, No 450-451 Le Van Viet Street, Tang Nhon Phu Ward, Ho Chi Minh City, Viet Nam

ARTICLE INFO

TYPE: Research Article
Received: 09/12/2025
Revised: 11/05/2026
Accepted: 13/05/2026
Published online: 15/05/2026
https://doi.org/10.47869/tcsj.77.4.6

* *Corresponding author*
Email: quanhv_ph@utc.edu.vn; Tel: +84986503205

Abstract. Uneven pavement surfaces increase the dynamic loads generated by moving vehicles. However, stability analyses of road embankments often neglect the influence of vehicle vibrations on slope stability. Therefore, considering the interaction between vehicles, pavement conditions, and slope response provides a more realistic evaluation of embankment stability. In this study, vehicle dynamics are simulated using a quarter-car model (QCM), pavement roughness is represented by the International Roughness Index (IRI), and slope stability is evaluated using the Fellenius method. Numerical simulations were conducted for an 8-m-high, 1:1 cut slope in homogeneous saturated cohesive soil under vehicle speeds of 20, 40, and 60 km/h. Four pavement roughness levels with IRI values of 2, 3, 5, and 7 were considered. Dynamic wheel loads for car and truck models were simulated in MATLAB-Simulink over 150 s using the Runge-Kutta integration method. The results show that the static factor of safety (FoS) is 2.05 for the car and 2.03 for the truck. Under dynamic loading with IRI=7, the FoS decreases to 1.96-2.00 for cars and 1.92-1.96 for trucks, depending on vehicle speed. The findings indicate that increasing pavement roughness and vehicle loads reduce slope stability and should be considered in road embankment design and assessment.

Keywords: Slope stability, factor of safety, Fellenius method, flexible pavement, dynamic wheel loads.

1. INTRODUCTION

Slope failures along road embankments remain a major hazard, especially in mountainous areas where high and sharply inclined cut slopes are common. Such failures can cause serious

economic losses and safety risks for road users. In practice, slope stability is further reduced by weather conditions that weaken soil strength and by dynamic loads generated by moving vehicles. The landslides that occurred during the late-2025 storms in the central and highlands regions of Viet Nam clearly demonstrate this problem.

Slope stability has been studied for many years using classical methods such as Fellenius, Bishop, and Janbu [1-4]. In recent decades, research has increasingly shifted to numerical modeling, especially the finite element method with software like Plaxis [5], GeoStudio [6], and Flac [7]. These tools allow analysis under complex soil and groundwater conditions and can include reinforcement measures.

Besides the traditional approaches, some studies use probabilistic methods [8], reliability analysis [9], and field monitoring data [10]. Research has also expanded from 2D models to 3D models for a more realistic representation of slope behavior [11]. In recent years, artificial intelligence techniques have also been applied to slope stability problems [12]. For dynamic loading, most studies focus on earthquake effects on road embankments [13,14]. Some authors have examined vehicle loads [15,16], but these works mainly use static loads or equivalent dynamic loads based on impact factors and do not consider the actual roughness of the pavement surface.

In Viet Nam, research on the stability of road embankment slopes has been carried out with a wide range of approaches. Several authors have applied numerical simulations using the discrete element method [17], the limit equilibrium method [18], or a combination of both [19]. Using the finite element method, [20] analyzed slope stability following the AASHTO-LRFD standard, while [21] incorporated artificial neural network models to improve prediction capability. Besides studies focusing on specific structures or reinforcement solutions, many authors have examined the influence of geotechnical and hydrogeological conditions [22-25]. Regarding dynamic loading, [26] assessed slope stability under vehicle loads based on the Russian Federation standard, where the loads were converted into equivalent static loads.

In studies on dynamic loads transmitted from vehicle axles to the pavement, the vehicle system can be modelled either as a full-vehicle system [27,28] or in a simplified form using a QCM [29]. To represent pavement surface irregularities, [30,31] improved the power spectral density model based on the ISO 8608 standard [32] by incorporating the *IRI* with a sinusoidal function, consistent with Vietnamese specifications. More recently, [33] further refined the road surface roughness (RSR) model by replacing the sinusoidal description with a Gaussian white noise (GWN) function.

Although many studies have investigated road embankment slope stability, most consider influencing factors separately and rely on simplified loading models. In practice, the dynamic loads generated by vehicle interaction with uneven pavement surfaces can be significantly higher than static loads. Therefore, incorporating these dynamic effects into slope stability analysis is essential to reflect actual operating conditions.

This study proposes an integrated approach that combines the Fellenius circular slip surface method with pavement self-weight and dynamic vehicle loads modelled using a QCM. The method provides a more realistic assessment of slope behaviour by accounting for vehicle type, speed, and RSR (represented by *IRI* value) with a GWN function. In this approach, the interaction between the vehicle model and the uneven pavement is simulated in MATLAB-Simulink to generate the dynamic loads. The model allows users to customize parameters such as vehicle loads, soil properties, and slope geometry.

2. PROBLEM FORMULATION

2.1. Fundamentals of the Fellenius method

Based on field observations, embankment and cut slopes in cohesive or layered soils typically exhibit rotational failure. The failure surface often follows a curved, see Fig. 1 (a), nearly cylindrical shape-steep at the crest (point C) and gradually flattening toward the toe (point A) [3,4]. Following the recommendations of TCVN 13346:2021 [34], the circular slip surface method of Fellenius is employed in this study to evaluate slope stability.

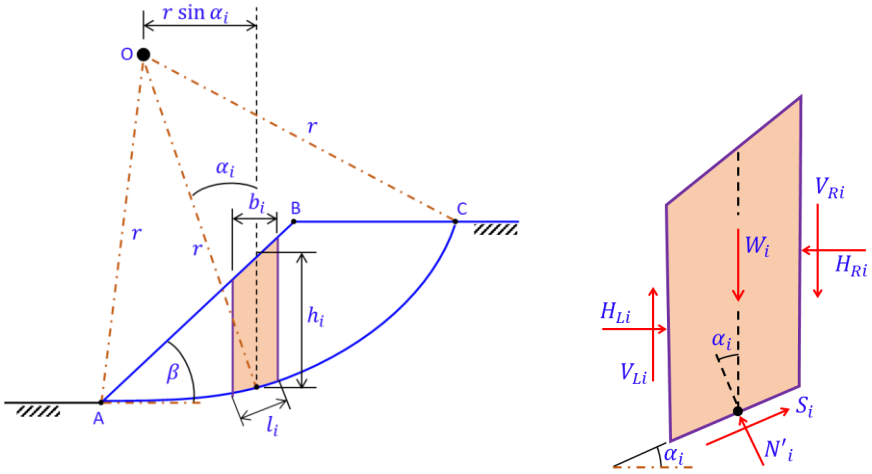

(a) (b)

Fig. 1. Fellenius method for slope stability analysis [3,4]: (a) Circular slip surface divided into vertical slices, (b) Free-body diagram of i^{th} slice.

In Fig. 1, the slip surface is divided into n vertical slices. Point O, which defines the center of the circular slip surface with radius r, is also used as the moment point to simplify the calculation of driving and resisting moments. For the i^{th} slice, b_i, h_i and l_i denote the slice width, the slice height measured along its centerline, and the base length, respectively. The inclination angle α_i defines the orientation of the base of the i^{th} slice relative to the horizontal.

Fig. 1 (b) shows the free-body diagram of the i^{th} slice. Here, W_i is the weight of the slice, $N_i = W_i \cos\alpha_i$ is the normal force, N'_i is the total normal force at the base, u_i is the pore water pressure. The effective normal force is given by $N'_i = N_i - u_i l_i$. S_i is the shear force along the base. H_{Li} and H_{Ri} are the left and right inter-slice normal forces, while V_{Li} and V_{Ri} are the corresponding inter-slice shear forces.

The factor of safety is a key parameter used to evaluate slope stability. It accounts for uncertainties in soil conditions, loading, and design experience, serving as a practical tool to ensure reliability under unknown or variable conditions. $\boldsymbol{FoS}$ is commonly defined using limit equilibrium based on stress, force, or moment balance. For circular slip surfaces and the method of slices, $\boldsymbol{FoS}$ is calculated as the ratio of resisting to overturning moments along the failure surface [1-4]:

$$\boldsymbol{FoS} = \frac{\boldsymbol{M_r}}{\boldsymbol{M_d}} \quad (1)$$

In Eq. (1), M_r is the sum of the resisting moments, M_d is the sum of the driving moments. In the Swedish method, which considers only moment equilibrium and neglects interslice shear forces, these moments are computed as:

$$\begin{cases} M_r = \sum_{i=1}^{n}[c_i' l_i + (W_i \cos\alpha_i - u_i l_i)\tan\varphi_i']r \\ M_d = \sum_{i=1}^{n}(W_i \sin\alpha_i)r \end{cases} \quad (2)$$

where the shear strength is defined by c_i', the effective cohesion; and φ_i' , the effective internal friction angle, both under effective stress conditions accounting for pore pressure.

By substituting Eq. (2) into Eq. (1), FoS based on global moment equilibrium can be expressed in the following simplified form:

$$\boldsymbol{FoS = \frac{c'\sum l_i + \gamma b_m \tan\varphi' \sum h_i \cos\alpha_i}{\gamma b_m \sum h_i \sin\alpha_i}} \quad (3)$$

A slope is stable if $FoS > 1$, at limit equilibrium if $FoS = 1$, and unstable if $FoS < 1$. According to [34], the required minimum FoS depends on the road classification: 1.30 for expressways, 1.25 for class I-II highways, 1.20 for class III-VI highways, 1.15 for provincial roads, and 1.10 for rural roads.

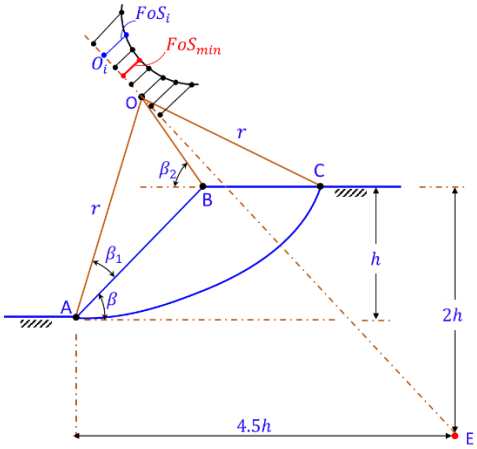

Figure 2. Illustration for determining the critical slip surface [3,4].

For a given slope, the FoS changes with the position of the slip surface, and the surface that gives the smallest FoS is the critical one. This minimum value $FoS_{\min}$ controls the stability of the slope and must meet the required safety level. Because only one slip surface gives this minimum value, finding it is the main goal of stability analysis. To make this process easier, W. Fellenius showed that the center of the critical circular slip surface lies on a line that passes through the slope toe [3]. The procedure is described below.

For slopes with high plasticity ($\varphi' \approx 0$) [3,4], the critical slip surface passes through the slope toe. The center O is found at the intersection of lines OA and OB, as shown in Fig. 2. Line OA makes an angle β_1 with the slope face, and line OB makes an angle β_2 with the slope crest. The values of β_1 and β_2 depend on the slope angle β, as given in Table 1.

Table 1. Values of β_1 and β_2 [3,4].

Slope gradient	Slope angle β	β_1	β_2
1 : 0.58	60°	20°	40°
1 : 1	45°	28°	37°
1 : 1.5	33.78°	28°	37°
1 : 2	26.57°	26°	35°
1 : 2.5	21.80°	25°	35°
1 : 3	18.43°	25°	35°
1 : 5	11.32°	25°	37°

When the soil internal friction angle φ' is greater than zero [3,4], the center of the critical

slip surface lies on the extension of segment OE, as shown in Fig. 2. In this case, several trial centers O_1, O_2, … are chosen along this extension, and the corresponding safety factors FoS_1, FoS_2, … are calculated using Eq. (3). At each trial center, a line segment is drawn to represent its FoS value. Connecting the ends of these segments forms a curve that shows how the safety factor changes. The lowest point on this curve gives the center of the critical slip surface.

2.2. Wheel load model

As mentioned in Section 1, a vehicle can be modelled as a quarter-car, half-car, or full-car system. For the 2D slope stability analysis along the road cross-section, the vehicle is considered only in the transverse direction. Using a half-car model in this direction requires simulating the uneven road profile between the two wheels, which complicates the analysis and may place one wheel outside the slip surface. Therefore, QCM is used in this study, see Fig. 3.

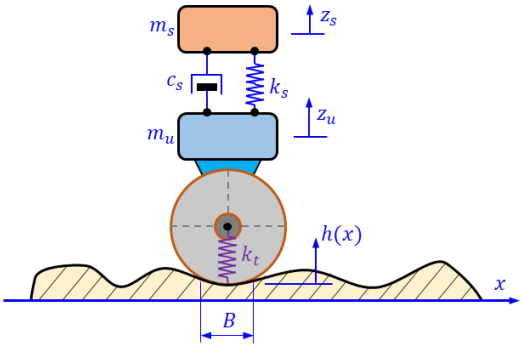

Figure 3. The quarter-car model [31].

In the QCM, the sprung mass m_s represents the vehicle body, while the unsprung mass m_u includes the wheel, tire, and half of the axle or suspension. The system has two degrees of freedom: the vertical displacement of the wheel mass z_u and the body mass z_s. The suspension has stiffness k_s and damping C_s, and the tire is modeled with stiffness k_t. The road profile input $h(x)$ is treated as a random function along the motion direction (x).

The motion equations of the QCM in Fig. 3 are derived from the free-body diagrams of the sprung and unsprung masses. The dynamic equilibrium is formulated using D'Alembert's principle. They are written as follows [30,31,33]:

$$\begin{cases} m_s\ddot{z}_s = -c_s(\dot{z}_s - \dot{z}_u) - k_s(z_s - z_u) \\ m_u\ddot{z}_u = c_s(\dot{z}_s - \dot{z}_u) + k_s(z_s - z_u) - k_t(z_u - h) \end{cases} \quad (4)$$

In this study, the road profile $h(x)$ is modeled by combining the randomness of GWN with the RSR described using an IRI profile, as proposed by [33]. The waveform of the GWN signal over time is shown in Fig. 4.

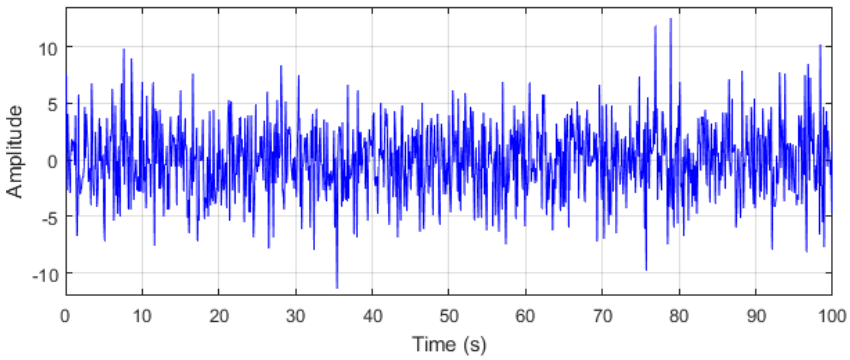

Fig. 4. Waveform of GWN function over 100 s.

Accordingly, the random road profile $h(x = ut)$ is a time-dependent function and is defined by the following differential equation [33]:

$$\dot{h}(t) = -2\pi n_{00} u h(t) + 2\pi n_0 \sqrt{1.63 K_0 IRI^2 u} w(t) \quad (5)$$

where $n_{00} = 0.01$, u is vehicle speed (assumed constant), $n_0 = 0.1$ m^{-1} is the reference spatial frequency, $w(t)$ is the GWN with a power spectral density of 1.0 and mean of 0.0, and $K_0 = 10^{-6}$ m^3.

The static force transmitted from the QCM to the pavement through the tire (F_s) is given by

$$F_s = (m_s + m_u)g \quad (6)$$

The additional dynamic force transmitted to the pavement (F_d) generated by the excitation from the RSR, is expressed as

$$F_d = k_t(z_u - h) \quad (7)$$

The total force transmitted to the pavement (F_t) obtained by adding the static component in Eq. (6) and the additional dynamic component in Eq. (7), is given by

$$F_t = k_t(z_u - h) + (m_s + m_u)g \quad (8)$$

where z_u is the tire's vertical displacement obtained by integrating Eq. (4), and $g = 9.81$ m/s^2 is the gravitational acceleration.

2.3. Self-weight of flexible pavement structures

For flexible pavement structures, the self-weight of each pavement layer generates a vertical distributed load acting on the road cross-section. The distributed mass w (kg/m²) of a pavement layer is computed from its unit weight and thickness as:

$$w_l = \rho_l t_l \quad (9)$$

where t_l is the layer thickness (m) and ρ_l is the material unit weight (kg/m³).

The total distributed mass is obtained by summing the contributions of all pavement layers. The corresponding gravitational load acting on the slope surface, expressed per unit length of the road cross-section, is:

$$q_p = g\sum w_{li} \quad (10)$$

For illustration, a low-grade flexible pavement structure for a two-lane roadway with an A2 surface layer, as specified in Appendix E of specification 22TCN 211:2006 [35], is considered. The pavement system consists of a double-seal asphalt surface layer (2 cm), a crushed stone base layer type I (16 cm), and a natural granular subbase type A (34 cm). The unit weights of these materials are taken as follows: asphalt surface 2400 kg/m³ (typical range 2300-2400 kg/m³), crushed stone base 2300 kg/m³, and natural granular subbase 2100 kg/m³ (typical range 2000-2200 kg/m³).

With the layer thicknesses of 2 cm, 16 cm, and 34 cm, respectively, and applying Eq. (9), the distributed mass of each layer is: $w_1 = 2400 \times 0.02 = 48$ kg/m^2, $w_2 = 2300 \times 0.16 = 368$ kg/m^2, and $w_3 = 2100 \times 0.34 = 714$ kg/m^2. Accordingly, applying Eq. (10), the total gravitational load per unit length of the road cross-section is: $q_p = (48 + 368 + 714) \times 9.81 = 11.09$ kN/m.

2.4. Integrated slope stability analysis under wheel loads and pavement self-weight

This section presents the proposed analytical model for evaluating the slope stability of a road embankment and determining the corresponding FoS. In this model, the embankment is subjected to wheel loads generated by the QCM, as described in Section 2.2, and the self-weight of the flexible pavement structure, also presented in Section 2.3. These loading components are incorporated into the Fellenius framework (Section 2.1) to compute the FoS and assess the combined effects of dynamic wheel loads and pavement self-weight on slope stability.

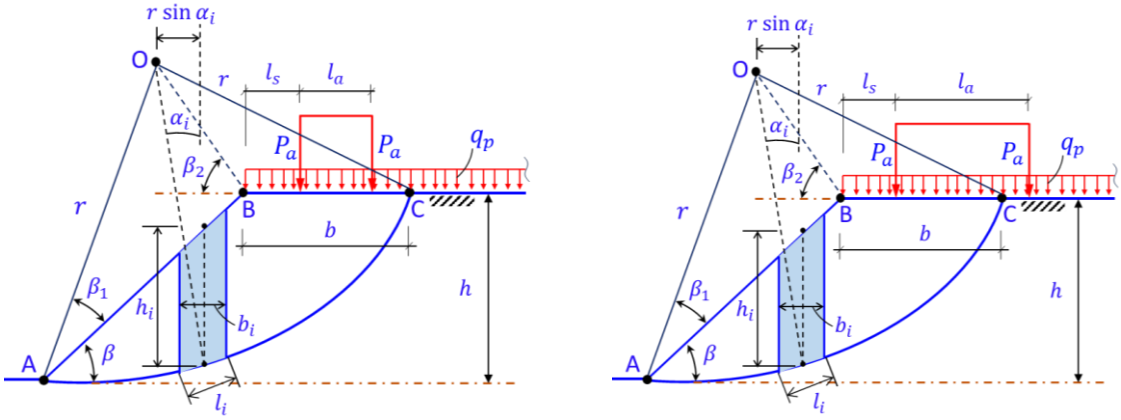

Fig. 5. Proposed analytical model for slope stability evaluation: (a) both loads inside, (b) one load inside the slip surface.

For simplicity, the following assumptions are adopted in this study: (i) the QCM wheel load is modelled as a concentrated vertical force P_a transmitted through the tire-pavement interface, and the vibration of the QCM does not alter the geotechnical properties of the embankment soil; (ii) the flexible pavement structure does not contribute to the slope's load-carrying capacity and is considered only through its self-weight, which is idealized as a uniformly distributed load q_p acting along the slope crest over a width b.

The slope and loading configuration are illustrated in Fig. 5. Each axle is assumed to carry two-wheel loads P_a, corresponding to the left and right tires, separated by a horizontal spacing l_a. For the considered axle, the left wheel load $P_a$is applied at a horizontal distance l_s from the slope crest (point B).

When the external loads P_a and q_p are considered, the slope becomes less stable because both loads increase the driving moment. As noted in section 2.1, the Fellenius method evaluates stability by taking moments about the slip-circle center O. In this model, the wheel load P_a and the pavement load q_p are not redistributed to individual slices. Instead, any part of these loads located inside the slip surface is added directly to the driving moment M_t.

The moment-equilibrium form of the Fellenius method can be rewritten as:

$$FoS = \frac{\sum_{i=1}^{n}[c_i' l_i + (W_i \cos\alpha_i - u_i l_i)\tan\varphi_i']}{\sum_{i=1}^{n}(W_i \sin\alpha_i) + \frac{M_O}{r}} \quad (11)$$

where M_O is the additional driving moment generated by the wheel load P_a and the pavement load q_p. All remaining parameters in Eq. (11) have been defined previously in section 2.1. The value of M_O is determined for two cases:

Case 1: $l_s + l_a \leq b$, see Fig. 5 (a), both wheel loads P_a of the considered axle lie inside the slip surface. The additional overturning moment M_O is defined as

$$M_O = q_p b\left(\frac{b}{2} + OB\cos\beta_2\right) + P_a(2l_s + l_a + OB\cos\beta_2) \quad (12)$$

Case 2: $l_s + l_a > b$, see Fig. 5 (b), the right-side wheel load P_a lies outside the slip surface (to the right of point C). The additional overturning moment M_O is defined as

$$M_O = q_p b\left(\frac{b}{2} + OB\cos\beta_2\right) + P_a(l_s + OB\cos\beta_2) \quad (13)$$

3. NUMERICAL INVESTIGATION

3.1. Input parameters and study cases

In this study, the basic parameters used to describe the random road profile $\boldsymbol{h(x)}$ in Eq. (5) are listed in Table 2. The study is conducted for a class-III road with speed limits of 60 km/h, 40 km/h, while a lower speed of 20 km/h is additionally considered to represent poor pavement conditions [36]. For this road class, the RSR is evaluated using the $\boldsymbol{IRI}$ values according to specification TCVN 8865:2011 [37], with four pavement quality levels: good ($\boldsymbol{IRI = 2}$), average ($\boldsymbol{IRI = 3}$), poor ($\boldsymbol{IRI = 5}$), and very poor ($\boldsymbol{IRI = 7}$).

Table 2. Basic input parameters for simulating the random road profile [33].

Parameter	K_0 (m^3)	n_0 (m^{-1})	n_{00}	u (km/h)	t (s)	B (m)	Δn	N
Value	10^{-6}	0.1	0.01	60, 40, 20	150	0.25	10^{-3}	4×10^3

The basic parameters of the QCM for two common vehicle types, car and truck, are listed in Table 3. In the QCM, the sprung mass $\boldsymbol{m_s}$ represents the portion of the vehicle body and payload supported by a single wheel, while the unsprung mass $\boldsymbol{m_u}$ includes the wheel, tire, and half of the axle assembly. Thus, the total mass associated with the single-wheel system is $\boldsymbol{m_s + m_u}$, and the corresponding static wheel load is $\boldsymbol{P_a = F_s = m_s + m_u}$ see the last row of Table 3.

Table 3. Fundamental dynamic parameters of the vehicle model [29-33].

Parameter	$\boldsymbol{m_s}$ (kg)	$\boldsymbol{m_u}$ (kg)	$\boldsymbol{k_s}$ (10^4 N/m)	$\boldsymbol{c_s}$ (10^4 Ns/m)	$\boldsymbol{k_t}$ (10^6 N/m)	$\boldsymbol{F_s}$ (kN)
Car	4000	550	32	1.0	1.7	44.64
Truck	4500	650	57	2.1	3.0	50.52

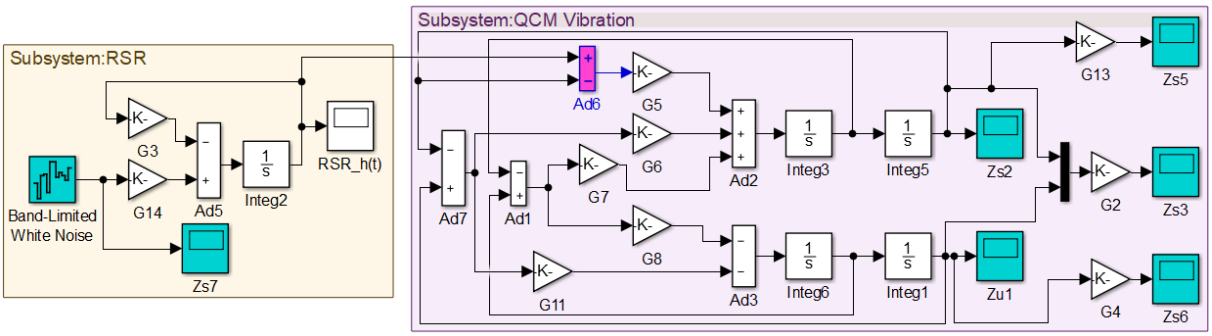

Fig. 6. Simulation of QCM-road surface interaction using MATLAB-Simulink.

Fig. 6 shows the simulation model implemented in MATLAB-Simulink. The RSR subsystem generates the road profile according to Eq. (3), while the QCM Vibration subsystem simulates the vertical motion of the vehicle model based on Eq. (4). The numerical integration is performed over 150 s with a 0.01 s time step using the Runge-Kutta method. Based on the parameters listed in Table 2, the simulated road profiles corresponding to vehicle speeds of 40

and 60 km/h under different pavement conditions ($\boldsymbol{IRI}$) are presented in Fig. 7. These road profiles, together with the vehicle parameters in Table 3, are used as input data for the simulation to obtain the QCM response, see Fig. 8.

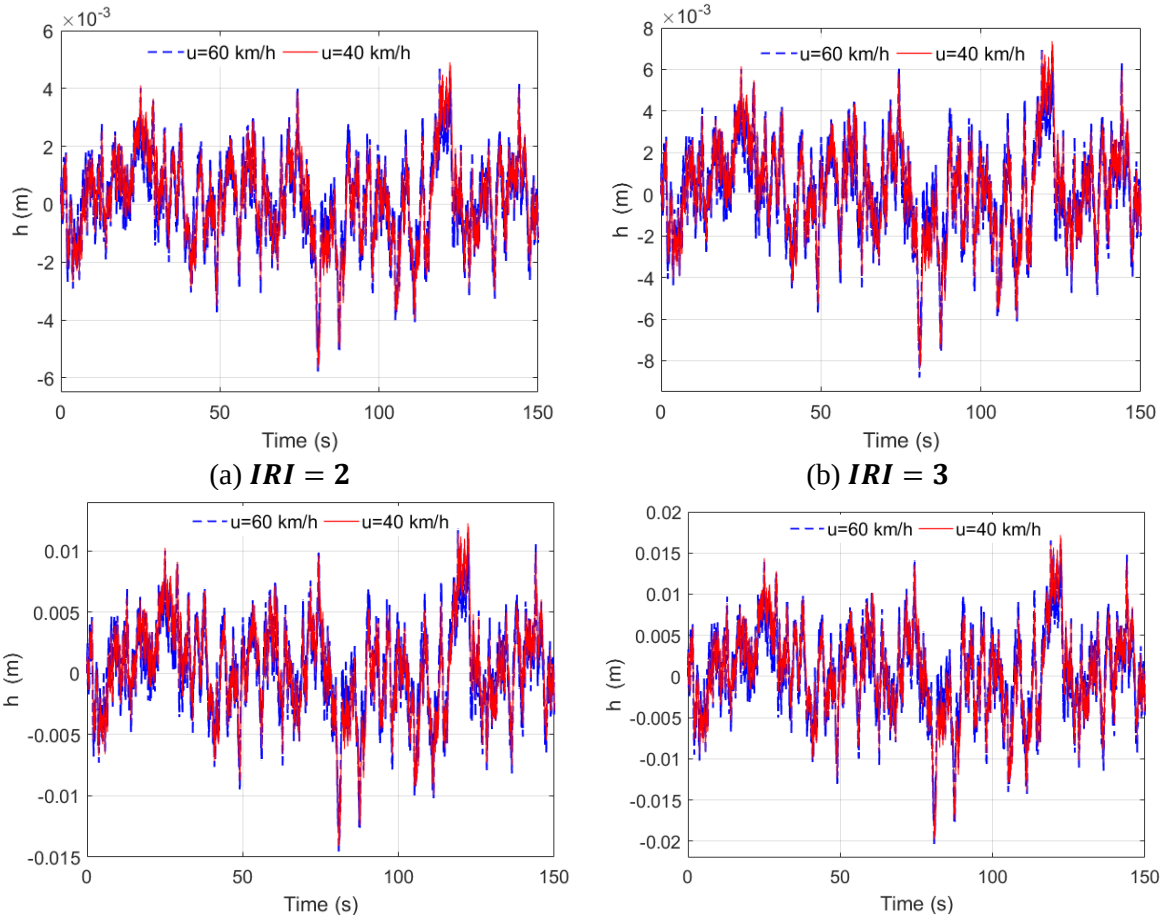

(a) $\boldsymbol{IRI = 2}$ (b) $\boldsymbol{IRI = 3}$

(c) $\boldsymbol{IRI = 5}$ (d) $\boldsymbol{IRI = 7}$

Fig. 7. Road surface profiles $\boldsymbol{h(x)}$ corresponding to different $\boldsymbol{IRI}$ values.

Fig. 8 presents the time response of the QCM model, illustrated for the case of $\boldsymbol{IRI = 5}$ at speeds of 60 and 40 km/h. The results from this numerical simulation are used in Eqs. (6)-(8) to determine the total force transmitted to the pavement ($\boldsymbol{F_t}$). Table 4 summarizes the maximum dynamic wheel loads on the pavement obtained from this analysis.

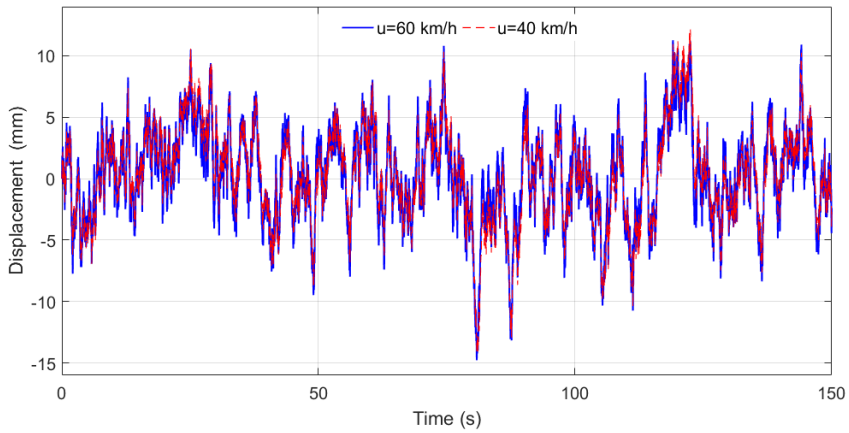

(a) Vibration of the sprung mass.

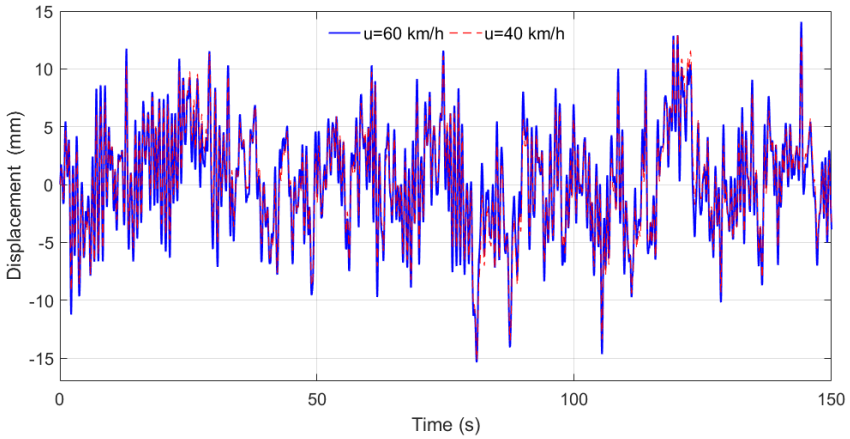

(b) Vibration of the unsprung mass.

Fig. 8. Time response of the QCM car model for $\boldsymbol{IRI = 5}$.

The results in Table 4 show that the maximum dynamic wheel loads are always higher than the static wheel loads of 44.64 kN for the car and 50.52 kN for the truck. For the car, $\boldsymbol{F_{t,max}}$ increases to about 1.1-1.5 times the static load as the $\boldsymbol{IRI}$ rises from 2 to 7; the truck shows a similar trend with an amplification of about 1.15-1.55. Vehicle speed also plays a clear role: the higher speed ($\boldsymbol{u = 60}$ km/h) consistently produces larger dynamic loads than $\boldsymbol{u = 40}$ km/h and $\boldsymbol{u = 20}$ km/h for all $\boldsymbol{IRI}$ levels. These results confirm that both road roughness and vehicle speed significantly intensify the wheel-pavement interaction force, especially under poor surface conditions ($\boldsymbol{IRI \geq 5}$).

Table 4. Maximum dynamic wheel load on the pavement.

$\boldsymbol{IRI}$	2			3		
$\boldsymbol{u}$ (km/h)	60	40	20	60	40	20
Vehicle	Maximum dynamic wheel load $F_{t,max}$ (kN)					
Car	50.95	49.82	48.29	54.11	52.41	50.11
Truck	58.32	57.00	55.02	62.21	60.23	57.27

Table 4 (continued). Maximum dynamic wheel load on the pavement.

$\boldsymbol{IRI}$	5			7		
$\boldsymbol{u}$ (km/h)	60	40	20	60	40	20
Vehicle	Maximum dynamic wheel load $F_{t,max}$ (kN)					
Car	60.43	57.59	53.76	66.55	62.91	57.41
Truck	70.00	66.65	61.77	77.79	73.10	66.27

According to specification TCVN 4054:2005 [36], the horizontal spacing between the two-wheel assemblies on the axle is taken as the overall vehicle width, resulting in $\boldsymbol{l_a = 2.5}$ m. This study considers a mountainous road with a design class III, the road consists of two lanes with a 6.0 m running width, 3.0 m per lane. The horizontal distance from the wheel load to the slope crest is taken as the minimum shoulder width, so $\boldsymbol{l_s = 1.5}$ m [36].

In this section, the uniformly distributed load induced by the low-grade flexible pavement structure is taken as the value computed in Section 2.3, giving $\boldsymbol{q_p = 11.09}$ kN/m. In this study, the analysis is limited to a single slope case, with the following characteristics. The cut slope of the road embankment (see Fig. 9) has a height of $\boldsymbol{h = 8}$ m and a slope ratio of 1:1. The slope soil is saturated cohesive soil, considered homogeneous. The geotechnical parameters are: unit

weight of soil $\boldsymbol{\gamma = 19}$ kN/m^3, undrained shear strength $\boldsymbol{c' = 65}$ kPa, and internal friction angle $\boldsymbol{\varphi' = 0^o}$ [4].

3.2. Slope stability analysis: results and discussion

Based on the slope ratio of 1:1 and the high-plasticity cohesive soil ($\varphi' = 0°$), the procedure outlined in Section 2 shows that the critical slip surface is a circular arc passing through the slope toe (point A). According to Table 1, for a slope angle of $\beta = 45°$, the center O of the critical slip circle is defined by the geometric angles $\beta_1 = 28°$ along OA and $\beta_2 = 37°$ along OB, see Fig. 9. From geometric relations, the radius of the slip circle is determined by:

$$r = \frac{h\sin(\beta+\beta_2)}{\sin\beta\sin(\beta+\beta_1+\beta_2)} = \frac{8\sin(45^o+37^o)}{\sin 45^o\sin(45^o+28^o+37^o)} = 11.93 \text{ m} \quad (14)$$

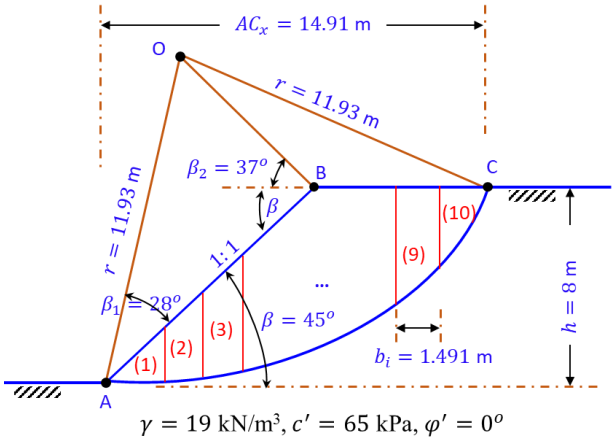

Fig. 9. Slope geometry and subdivision of the critical slip surface.

By geometric construction, the slope width is $b = 6.91$ m, and the horizontal length of segment AC is $AC_x = 14.91$ m. With the pavement dimensions, where $l_s = 1.5$ m and $l_a = 2.5$ m, their sum is $l_s + l_a = 4.0$ m, which is smaller than the slope width $b = 6.91$ m. This means that both wheel loads of the considered axle are located entirely within the investigated slip surface.

Using the slice method presented in Section 2, the sliding mass is divided into vertical slices of equal width. In this study, each slice has a width of $b_i = \frac{AC_x}{10} = \frac{14.91}{10} = 1.491$ m. The numbering of the slices is shown in Fig. 9. Since the soil is homogeneous and the slice widths are equal, Eqs. (3) and (12) becomes:

$$FoS = \frac{c'\sum l_i + \gamma b_m \tan\varphi' \sum h_i \cos\alpha_i}{\gamma b_m \sum h_i \sin\alpha_i} \quad (15)$$

$$FoS = \frac{c'\sum l_i + \gamma b_m \tan\varphi' \sum h_i \cos\alpha_i}{\gamma b_m \sum h_i \sin\alpha_i + \frac{M_O}{r}} \quad (16)$$

Table 5. Calculation of parameters for each slice.

No. slice	α_i (deg)	h_i (m)	$\sin\alpha_i$	$\cos\alpha_i = \sqrt{1-\sin^2\alpha_i}$	$h_i \sin\alpha_i$ (m)	$h_i \cos\alpha_i$ (m)	l_i (m)
1	-13.32	0.92	-0.23	0.97	-0.21	0.90	1.53
2	-6.04	2.69	-0.11	0.99	-0.28	2.68	1.50
3	1.14	4.24	0.02	1.00	0.08	4.24	1.49
4	8.34	5.92	0.14	0.99	0.86	5.86	1.51
5	15.68	6.65	0.27	0.96	1.80	6.40	1.56

No. slice	α_i (deg)	h_i (m)	$\sin\alpha_i$	$\cos\alpha_i = \sqrt{1-\sin^2\alpha_i}$	$h_i \sin\alpha_i$ (m)	$h_i \cos\alpha_i$ (m)	l_i (m)
6	23.30	7.52	0.40	0.92	2.97	6.91	1.62
7	31.30	6.76	0.52	0.85	3.51	5.78	1.74
8	40.12	5.69	0.64	0.76	3.67	4.35	1.95
9	50.62	4.13	0.77	0.63	3.19	2.62	2.35
10	63.40	1.94	0.89	0.45	1.73	0.87	3.56
Total values (m):					17.32	40.60	18.81

Substituting the values from Table 5 into Equation (15) gives $FoS = 2.49$. According to [4], the full-mass slip method yields $FoS_r = 2.48$, giving a difference of $\Delta = \frac{FoS - FoS_r}{FoS} = \frac{2.49-2.48}{2.49} \times 100 = 0.4\%$. This very small deviation ($< 0.5\%$) confirms that the calculation method used in this study is sufficiently accurate.

With the geometric dimensions of the axle and the slope, together with the static wheel loads from Table 3, where $P_a = F_s$. Eq. (12) is used to calculate the additional sliding moment caused by the pavement structural load and the static axle load of car model: $M_O = 11.09 \times 6.91(\frac{6.91}{2} + 4.51) + 44.64(1.5 + 4.51) + 44.64(1.5 + 2.5 + 4.51) = 1258.51$ kNm. Substituting this value into Eq. (16), one gets: $FoS = \frac{65 \times 18.81 + 19 \times 1.491 \times 0.0 \times 40.60}{19 \times 1.491 \times 17.32 + \frac{1258.51}{11.92}} = 2.05$. Similarly, using the static wheel loads of truck model in Table 3 and the dynamic wheel loads in Table 4, the corresponding FoS values are summarized in Table 6, where $P_a = F_{t,max}$.

Table 6. Summary of $\boldsymbol{FoS}$ values under static and dynamic loads.

$\boldsymbol{IRI}$		2			3			Static $\boldsymbol{FoS}$
$\boldsymbol{u}$ (km/h)		60	40	20	60	40	20	
Vehicle		Dynamic $\boldsymbol{FoS}$						
Car	Value	2.02	2.03	2.04	2.01	2.02	2.03	2.05
	Difference $\boldsymbol{FoS_{static} - FoS_{dynamic}}$	0.03	0.02	0.01	0.04	0.03	0.02	
Truck	Value	1.99	2.00	2.01	1.98	1.99	2.00	2.03
	Difference $\boldsymbol{FoS_{static} - FoS_{dynamic}}$	0.04	0.03	0.02	0.05	0.04	0.01	

Table 6 (continued). Summary of $\boldsymbol{FoS}$ values under static and dynamic loads.

$\boldsymbol{IRI}$		5			7			Static $\boldsymbol{FoS}$
$\boldsymbol{u}$ (km/h)		60	40	20	60	40	20	
Vehicle		Dynamic $\boldsymbol{FoS}$						
Car	Value	1.99	2.00	2.01	1.96	1.98	2.00	2.05
	Difference $\boldsymbol{FoS_{static} - FoS_{dynamic}}$	0.06	0.05	0.04	0.09	0.07	0.05	
Truck	Value	1.95	1.96	1.98	1.92	1.94	1.96	2.03
	Difference $\boldsymbol{FoS_{static} - FoS_{dynamic}}$	0.08	0.07	0.05	0.11	0.09	0.07	

From the results in Table 6, it is observed that:

a. Effect of dynamic loading: The FoS under dynamic loading is consistently lower than that under static loading for both the car and the truck. The magnitude of this reduction increases with pavement roughness (higher IRI). For the car moving at 60 km/h, the FoS decreases by

0.03 at $IRI = 2$ and by 0.09 at $IRI = 7$. For the truck moving at 60 km/h, the corresponding reductions are 0.04 and 0.11, respectively. These results show that dynamic wheel loads have a stronger influence on slope stability as pavement conditions deteriorate, with the effect being more pronounced for heavier vehicles; given that the allowable difference in the safety factor for different road classes is about 0.05 according to [34], the observed reduction in dynamic FoS is noteworthy.

b. Effect of vehicle speed: For a given pavement condition, the FoS decreases when vehicle speed increases. The FoS at 60 km/h is consistently lower than that at 40 and 20 km/h. At $IRI = 2$, 3, and 5, the reduction in FoS due to the higher speed is approximately 0.01 for both vehicles. At $IRI = 7$, this reduction increases to 0.02, indicating that rougher pavements amplify the influence of vehicle speed on slope stability.

c. Comparison between car and truck: In all evaluated scenarios, the truck produces a lower FoS than the car because its greater axle load generates higher dynamic forces and larger inertial effects. For example, at $IRI = 7$ and $u = 60$ km/h, the FoS is 1.96 for the car and 1.92 for the truck, confirming the greater destabilizing effect of heavy vehicles.

4. CONCLUSION

This study proposed an integrated analytical model for evaluating slope stability of road embankments, combining the Fellenius circular slip surface method with the effects of flexible pavement self-weight and dynamic wheel loads modelled by a quarter-car system. This approach allows a more realistic assessment of slope stability under operational conditions, capturing the influence of vehicle type, speed, and pavement roughness on the driving moments.

A numerical simulation was performed for an 8 m-high, 1:1 cut slope composed of homogeneous saturated cohesive soil, under a mountainous class-III road with speed limits of 20, 40 and 60 km/h and pavement roughness levels $IRI = 2$, 3, 5, and 7. Vehicle loads were modeled using a quarter-car system for both a car and a truck, and dynamic responses to road irregularities were simulated in MATLAB-Simulink over 150 s using Runge-Kutta integration with 0.01 s time steps. The results confirm that dynamic loading reduces the FoS compared with static conditions, with reductions increasing from 0.03 to 0.09 for the car and from 0.04 to 0.11 for the truck as pavement roughness rises from $IRI = 2$ to 7. Vehicle speed also affects stability, where raising the speed from 20, 40 to 60 km/h decreases FoS by about 0.01 at $IRI = 2$ to 5 and by 0.02 at $IRI = 7$.

The findings confirm that increasing pavement roughness, vehicle speed, and axle load leads to a reduction in slope stability. Future studies should extend the model to 3D slopes with full-car systems, non-homogeneous soils, and additional environmental influences such as rainfall, variations in pore-water pressure, and seismic loading.

The findings confirm that increasing pavement roughness, vehicle speed, and axle load leads to a reduction in slope stability. However, the present study considers a simplified slope configuration, which does not fully represent the complexity of real road embankments. In future work, numerical analyses should investigate road embankment structures with different slope angles, multilayered soil profiles, and varying groundwater table depths to better capture realistic geotechnical conditions. Future studies should also extend the model to 3D slopes with full-car systems or longitudinal 2D vehicle models, and consider additional environmental influences such as rainfall, variations in pore-water pressure, and seismic loading.

ACKNOWLEDGMENT

This research is funded by University of Transport and Communications (UTC) under grant number T2026-PHII_CT-008.

REFERENCES

[1]. L. W. Abramson, T. S. Lee, S. Sharma, G. M. Boyce, Slope stability and stabilization methods, John Wiley & Sons, Boca Raton, 2001.
[2]. Y. M. Cheng, C. K. Lau, Slope stability analysis and stabilization: New methods and Insight, CRC press, New York, 2008.
[3]. B. A. Dinh, Soil Mechanics, Construction Publishing House, Ha Noi, 2006. (in Vietnamese)
[4]. N. D. Dung, Soil Mechanics, Construction Publishing House, Ha Noi, 2007. (in Vietnamese)
[5]. Online: Bentley-Geotechnical Engineering, https://www.bentley.com/software/geotechnical-engineering/. (accessed on 08 December 2025)
[6]. Online: GeoStudio-Support Portal, https://www.geoslope.support/home/#. (accessed on 08 December 2025)
[7]. E. M. Dawson, W. H. Roth, Slope stability analysis with Flac, In Flac and numerical modeling in geomechanics, CRC Press, Ontario, 2020.
[8]. R. Chakraborty, A. Dey, Probabilistic slope stability analysis: State-of-the-art review and future prospects, Innovative Infrastructure Solutions, 7 (2022) 177. https://doi.org/10.1007/s41062-022-00784-1
[9]. L. Wang, C. Wu, L. Tang, W. Zhang, S. Lacasse, H. Liu, L. Gao, Efficient reliability analysis of earth dam slope stability using extreme gradient boosting method, Acta Geotechnica, 15 (2020) 3135-3150. https://doi.org/10.1007/s11440-020-00962-4
[10]. N. Kardani, A. Zhou, M. Nazem, S. L. Shen, Improved prediction of slope stability using a hybrid stacking ensemble method based on finite element analysis and field data, Journal of Rock Mechanics and Geotechnical Engineering, 13 (2021)188-201. https://doi.org/10.1016/j.jrmge.2020.05.011
[11]. T. Li, W.Gong, H. Tang, L. Zhang, A meshed kinematical approach for 3D slope stability analysis, International Journal for Numerical and Analytical Methods in Geomechanics, 46 (2022) 2913-2930. https://doi.org/10.1002/nag.3433
[12]. W. Gao, S. Ge, A comprehensive review of slope stability analysis based on artificial intelligence methods, Expert Systems with Applications, 239 (2024) 122400. https://doi.org/10.1002/nag.3433
[13]. C. Y. Chen, H. W. Chen, W. C. Wu, Numerical modeling of interactions of rainfall and earthquakes on slope stability analysis, Environmental Earth Sciences, 80 (2021) 524. https://doi.org/10.1007/s12665-021-09855-5
[14]. Z. Ma, H. Liao, F. Dang, Y. Cheng, Seismic slope stability and failure process analysis using explicit finite element method, Bulletin of Engineering Geology and the Environment, 80 (2021) 1287-1301. https://doi.org/10.1007/s10064-020-01989-3
[15]. Y. Zhang, H. Jiang, G. Bai, B. Han, Coupling action of rainfall and vehicle loads impact on the stability of loess slopes based on the iso-water content layer, Earthquake Research Advances, 2 (2022) 100143. https://doi.org/10.1016/j.eqrea.2022.100143
[16]. P. Rao, J. Meng, J. Cui, W. Fen, S. Nimbalkar, Z. Liu, Stability analysis of unsaturated soil pit under vehicle load, Geotechnical and Geological Engineering, 42 (2024) 4987-5001. https://doi.org/10.1007/s10706-024-02825-1
[17]. T. N. T. Hai, N. T. Vu, Numerical analysis of slope stability by discrete element method, Journal of Science and Technology in Civil Engineering, 2 (2022) 21-28. (in Vietnamese)
[18]. T. N. M. Tam, K. P. Q. Ta, T. V. M. Thien, Bearing capacity analysis of shallow foundations on slopes using limit equilibrium theory, Journal of Science and Technology in Civil Engineering, 3-4 (2013) 1-9. (in Vietnamese)
[19]. N. T. Kien, T. N. Linh, N. M. Quan, Application of finite element method and machine learning for analyzing slope reinforcement with a row of vertical piles, Journal of Building Materials Research and Development, 15 (2025) 232-239. (in Vietnamese) https://doi.org/10.54772/jomc.03.2025.1007
[20]. C. T. Linh, N. T. Quang, Analysis of embankment slope stability by limit equilibrium method and

finite element method according to AASHTO-LRFD, The University of Danang-Journal of Science and Technology, 19 (2021) 69-74. (in Vietnamese)
[21]. L. T. Nghia, M. C. Huy, N. H. T. Hau, T. C. Anh, T. V. Ninh, P. T Kien, N. M. Trung, Slope stability assessment using the finite element method and artificial neural network models, Journal of Materials and Construction, 15 (2025), 201-205. (in Vietnamese) https://doi.org/10.54772/jomc.03.2025.1013
[22]. P. Kien, T. V. Thien, Slope stability assessment of clay slopes considering long-term deformation behavior, Journal of Transport, 1-2 (2025) 69-72. (in Vietnamese)
[23]. M. T. Le, Applying soil-water characteristic curves to slope stability analysis, Master Thesis, University of Science and Technology-The University of Da Nang, Da Nang, Viet Nam, 2023. (in Vietnamese)
[24]. N. T. Q. Nhu, T. N. K. Ton, Application of Neo-Web materials for slope stabilization in road embankment construction, Journal of Transport, 6 (2023) 95-98. (in Vietnamese)
[25]. N. V. Du, N. V. Hung, P. N. Bay, Assessment of the impact of soil physical properties and vegetation on embankment stability, Transport and Communications Science Journal, 76 (2025) 361-372. (in Vietnamese) https://doi.org/10.47869/tcsj.76.3.13
[26]. N. V. Du, N. V. Hung, A study on the influence of dynamic loads on the stability of road embankment slopes, Journal of Transport, 64 (2024), 26-29. (in Vietnamese)
[27]. V. V. Tan, T. M. Hung, O. Sename, An investigation into the ride comfort of buses using an air suspension system, International Journal of Heavy Vehicle Systems, 28 (2021) 184-205. https://doi.org/10.1504/IJHVS.2021.115595
[28]. V. V. Tan, Two-Layer Parallel Fuzzy Logic Controller Design for Semiactive Suspension System with a Full Car Model, Shock and Vibration, 2023 (2023) 7020462. https://doi.org/10.1155/2023/7020462
[29]. V. V. Tan, N. V. Vinh, P. T. Thang, A. Mihaly, P. Gaspar, optimizing a Hybrid controller for automotive active suspension system by using genetic algorithms with two high level parameters, IEEE Access, 12 (2024), 172451-172464. https://doi.org/10.1109/ACCESS.2024.3499352
[30]. H. V. Quan, T. M. Canh, L. V. Phuc, Vehicle model dynamic analysis under random excitation of uneven pavement as measured by the international roughness index, Transport and Communications Science Journal, 8 (2023) 866-880. (in Vietnamese) https://doi.org/10.47869/tcsj.74.8.2
[31]. H. V. Quan, L. V. Phuc, A simple formula in calculating the flexible pavement life based on the influence of dynamic vehicle-uneven pavement interaction, Transportation Infrastructure Geotechnology, 12 (2025) 82. https://doi.org/10.1007/s40515-025-00538-3
[32]. M. Agostinacchio, D. Ciampa, S. Olita, The vibrations induced by surface irregularities in road pavements-a Matlab® approach, Eur. Transp. Res. Rev, 6 (2014) 267-275. https://doi.org/10.1007/s12544-013-0127-8
[33]. H. V. Quan, Evaluating dynamic tire pressure variations on uneven road surfaces, Vietnam Journal of Science and Technology, 62 (2025) 601-611. https://doi.org/10.15625/2525-2518/19409
[34]. Viet Nam National Standard, TCVN 13346:202: The landslide prevention engineering on road requirements for investigation and design. (in Vietnamese)
[35]. National Specification of Vietnam, 22TCN 211-06: Flexible Pavement Design-Specification and Guidelines. (in Vietnamese).
[36]. National Specification of Vietnam, TCVN 4054:2005: Highway-Specifications for design. (in Vietnamese)
[37]. National Specification of Vietnam, TCVN 8865:2011: Method for Measuring and Assessment roughness by International Roughness Index. (in Vietnamese)